Computational ballistic analysis of the cranial shot to John F. Kennedy

C. Then[a,*], K. Nelson[b], T.J. Vogl[a,c], K.E. Roth[d]

[a] *Center of Biomedical Engineering CBME, Frankfurt/M., Germany*

[b] *Department of Vascular and Endovascular Surgery, Goethe University Hospital Frankfurt/M., Germany*

[c] *Department of Diagnostic and Interventional Radiology, Goethe University Hospital, Frankfurt/M., Germany*

[d] *Center of Orthopedic and Trauma Surgery, Johannes Gutenberg University, Mainz, Germany*

*Corresponding author

E-mail address: christophe.then@t-online.de (C. Then)

ORCID: 0000-0001-5247-0547

Acknowledgements

The authors would like to thank Luke Haag of Forensic Science Services, Carefree, AZ, USA for providing information about the Carcano bullet ballistics.

Abstract

Almost 60 years after the assassination of John F. Kennedy in 1963 the majority of Americans are still reluctant to believe the official reports of commissions from 1964 and again in 1976 that determined the direction of the shot resulting in the fatal head injury. Long-withheld, confidential government files released in 2017 reignited the controversy.

The present investigation computationally simulated projectile-skull impacts from the direction specified in official reports and from three other directions. Detailed geometric models of the human head and ammunition, as well as known parameters from the assassination site served as the supportive base for analysis. Constitutive mathematical models for the impact of projectile material with skull tissues at supersonic speed were employed to analyze bone and bullet fragmentation mechanics.

Simulated fracture characteristics of the bone and the bullet were compared with photographic and X-ray evidence. The most likely origin of the fatal shot was determined based on the degree of corresponding deformation and fragmentation between simulation and documented evidence. Computational corroboration could be established as physically consistent with high-speed impact from the rear, as established by the official commissions. Simulations of three other speculative shot origins did not correspond to the documented evidence.

Keywords: Cranial gunshot, bone and bullet fracture mechanics, finite element simulation

Contents

1 Introduction

2 Methods

2.1 Potential shot origins

2.2 Initial conditions prior to bullet impact

2.3 Projectile geometry and mass distribution

2.4 Skull geometry

3 Constitutive modeling and FE representation

3.1 Projectile model

3.2 Head model

3.2.1 Scalp skin

3.2.2 Skull bone

3.2.3 Cerebrospinal fluid

3.2.4 Brain tissue

4 Forensic evidence

4.1 Bullet fragments

4.2 Autopsy X-rays of Kennedys' head

4.3 Autopsy photographic evidence

5 Results

5.1 Simulated shot from the TSBD-direction

5.2 Simulated shot from the GK-direction

5.3 Simulated shot from the SD-direction

5.4 Simulated shots *from the SK-direction*

5.5 Simulated post-impact phase: head and upper body motion

6 Discussion

7 Conclusions

Appendix

Simulated post-impact phase: bullet fragment traces resulting from a shot from the TSBD

References

Abbr.: TSBD: Texas School Book Depository. GK: Grassy Knoll. SD: Storm drain. SK: South Knoll.

1 Introduction

The President's Commission on the Assassination of President Kennedy, unofficially the *Warren Commission*, released its final report in 1964 and attributed the assassination of President John F. Kennedy (JFK) to three shots fired from a single marksman behind the presidential limousine with two bullets striking the president from the rear. While the first shot missed, the second shot caused a neck wound to Kennedy. The third and fatal shot hit Kennedy in the head [1].

Controversy concerning the commission report arose due to a physician in the overall disarray describing the neck wound from the second shot as a bullet entrance from the front throat [2-5]. Considerable doubt regarding the shot direction was further raised by the testimony of over 40 eye witnesses, including treating doctors, who unanimously reported a large wound in the right back of Kennedy's head [5-9], contradicting the official version of a large wound in the temple region of the right frontal bone [6]. Further contradiction was added by the film from a civilian bystander [10], known as the *Zapruder Film*, showing the president's head snapping violently backward upon impact with the third shot. Intuitive interpretation of this backward movement led to a lay verdict that the projectile must have come from the front.

Due to diminishing public trust in the 1964 report and to resolve controversy, the United States House of Representatives Select Committee on Assassinations (HSCA) was convened as a second official panel in 1976. The HSCA confirmed the main findings of the Warren Commission and concluded that JFK was hit by two shots from behind him. However, it was also concluded that with "high probability" at least two gunmen were involved [11]. Intense controversy thus remained and conspiracy theories still linger, many of them involving other or multiple possible shot directions as considered likely by the HSCA report [12]. In opposition to both official commissions that located the 6th floor of the Texas School Book Depository building to the rear of President Kennedy as the origin of the fatal shot, various conspiracy theories claim different sites as shooter locations [6,7,13-17]. The disagreement about the exact circumstances of the assassination, including possible shot directions, is reflected to date in over 40,000 published books and articles [18].

The present investigation compares the official findings related to the fatal shot origin to conspiracy related hypotheses by using state-of-the-art numerical software simulating the complex scenario of high-dynamic three-dimensional nonlinear bullet-skull penetration. Various shot origins were simulated using detailed models of the head and the bullet and these were compared with photographic and forensic evidence, particularly the documented

sharp skull bone defect in Kennedy's right temple and the deformed and fragmented bullet jacket. Also, the mechanical cause of the non-intuitive violent post-impact retrograde head snap is elucidated.

2 Methods

2.1 Potential shot origins

At time of the fatal shot John F. Kennedy was situated in the presidential limousine on Elm Street in Dallas, Texas, cf. Fig.1 position (L). While the official report states that the Texas School Book Depository (TSBD) behind the presidential limousine was the origin of the fatal shot, conspiracy related hypotheses propose the following other locations as possible shot origins [6,7,13-17]: 1. the Grassy Knoll (GK), an elevated site to the right of the limousine, 2. the South Knoll (SK) to the front/slight left and 3. a storm drain (SD) to the slight right front of the limousine. The SK-site included three potential shooter locations, Fig1. labels (1), (2), (3). Traces from these locations to the current position of Kennedys' head are depicted to scale in Fig.1 and, also to scale but enlarged in Fig.2. Geometric details of Fig.1 and Fig.2 including traces from the potential shot origins were generated using schematic scale drawings together with a true to scale top view picture of the assassination site [12,19,20]. Data of the presidential limousine was based on a commercially available digital model as well as scale drawings [5,12].

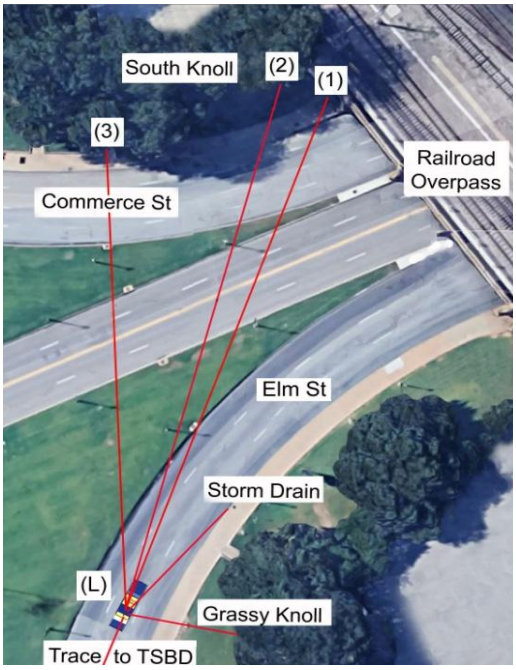

Fig.1 True to scale top view photo with superimposed limousine model (L) and potential shot directions/traces to various sites at time of the fatal shot (Credit: 2021 Google Inc.)

All drawings were digitalized employing CreoParametric (PTC, MA, USA). Digitalized data was assembled in one model using HyperWorks software package (Altair, MI, USA). Trace lengths and declinations were deduced from the assembled model. They are listed in section 2.2.

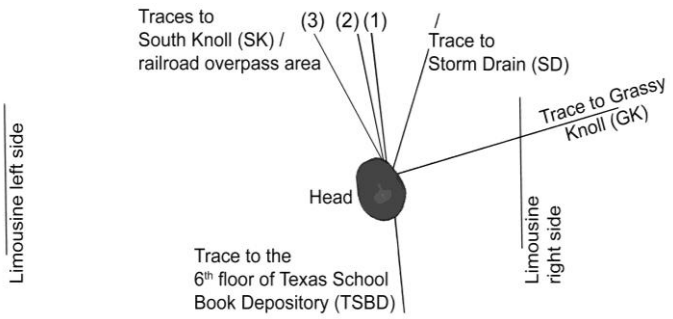

Fig.2 True to scale schematic: Kennedys' head position relative to potential shot directions at time of the fatal shot

Shot traces were also used to spatially orient the bullet model relative to the head model in the simulation.

2.2 Initial conditions prior to bullet impact

The Carcano projectile, officially identified as the assassination ammunition [5,12], was determined to have an average muzzle velocity of 670 m/s with a clockwise twist rate of 1 x 21.5 cm [21]. The velocity is 638 m/s after travelling 24 m, which was the distance between JFK's head and the location of the SD, 633 m/s at a distance of 30 m from the fence on the GK, and approximately 590 m/s at a distance of 82 m from the 6th floor window of the TSBD, and an average 574 m/s for a distance of 80 - 90 m for the SK-area [5,19,21,22]. The trajectory declination angles were approximately 0.2°- 5°, 5°, 8°, and 15° from the SK, GK, SD, and TSBD, respectively, to the position of Kennedys' head. The ground distance to the 6th floor of the TSBD was assumed 18.5 m, the approximate vertical distance from the GK fence to street level 2.5 m, 0 m from the SD and 4 - 5 m from the SK area. These distances and angles determine spatial bullet position and orientation to the head.

Approximate spatial orientation of the head relative to the limousine was based on Frame #312 of the *Zapruder Film*, Figs.3a, depicting the scene immediately prior to the fatal head shot. Based on Fig.3b - a blow-up of Fig.3a - Kennedy's head and the head model used for simulation were digitally superimposed, aligned and orientated.

Fig.3a Frame #312: Limousine passengers immediately prior to the fatal head shot: fond right: JFK

Fig.3b Blow-up detail: superposition and image alignment with the head model (white)

Credit: *Zapruder Film* (Renewed 1995) The Sixth Floor Museum at Dealey Plaza

Positioning of the bullet and head model with respect to a shot from the TSBD was based on the digitalized trajectory as well as on information from the Clark and HSCA forensic panel report stating that the wound on the back of JFK's head was located about 100 mm above the external occipital protuberance, and between 18 - 25 mm to the right of the head midline [12,23]. Bullet positioning for the other potential shot origins - SK, SD and GK - was based on trace/trajectory geometries as previously delineated.

2.3 Projectile geometry and mass distribution

To obtain computer-aided design data of the Carcano projectile (6.5×52 mm "Parravicini-Carcano"), scale drawings [24] were digitalized. In addition, bullets samples were milled to obtain section cut samples, Fig.4a. Using a 3D-digital microscope bullet dimensions were verified: jacket outer length and diameter at the bearing surface were 30.4±0.2 mm and Ø = 6.6±0.2 mm, respectively.

Fig.4a Parravicini-Carcano bullet: mid plane section cut of jacket and lead core

Fig.4b Bullet nose detail: lead core with copper-alloy jacket

Jacket thickness varied over the length: 0.42±0.2 mm (bearing surface) to 0.85±0.2 mm (nose), Fig.4b. After digital model generation, the mean volumes of the jacket and core were found to be 260 mm³ and 714 mm³, respectively, and the bullet's mass was 10.4 g, in accordance with official specifications [5]. Digital volumes together with the densities listed in Tables 3,4 yielded a lead core mass of 8.1 g and a jacket mass of 2.3 g.

Contact surfaces of jacket and core are loosely connected. The jacket is open at the base, Fig.4a-bottom. Mechanically, this design is described as a "single cell, one-end closed tube structure with closed thin wall section". This is important to comprehend bullet stability and deformation behavior.

2.4 Skull geometry

Precise data specifically pertaining to Kennedy's head anatomy do not exist. Thus, a human skull exhibit, as well as a plastinated brain, were scanned using computed tomography (CT) to acquire digitalized anatomical data. Scan images were reconstructed using MIMICS software (Materialise, Leuven, Belgium) providing digital data used for finite element (FE) head modeling including cortical and cancellous bone, cerebrospinal fluid (CSF) volume, brain and skin tissue. Thickness of the parietal/ occipital bone was estimated from Kennedys' autopsy X-ray photographs together with his head circumference, i.e. 61 cm [12,25]. The FE model was scaled accordingly to fit these values.

3 Constitutive modeling and FE representation

The peak strain rate corresponding to a typical defense-related ballistic impacts is in the order of 10^5-10^6 s^{-1}. Material data in that range is sparse. Bullet, scalp skin, bone, and brain tissue material properties thus were deduced based on the literature.

3.1 Projectile model

Substantial controversy surrounds the bullet's alloy composition [12,26,27]. In this report it was assumed that the bullet jacket consisted of 90% copper and 10% zinc, and the soft core consisted of common lead [12].

To realistically simulate bullet fragmentation behavior, adequate material modeling is essential. Jacket material was modeled using a modified version of the Johnson-Cook constitutive relation [28]. This model expresses the equivalent flow stress σ_y, Eq.(1), considering the effects of rate-independent strain hardening represented by a power law together with strain-rate dependence and thermal softening:

$$\sigma_y = \left(A + B\varepsilon_p^n\right)\left(1 + \bar{\dot{\varepsilon}}_p\right)^C (1 - \bar{T}^m) \tag{1}$$

with *A*, *B*, *C*, *m*, and *n* being experimentally determined constants, ε_p is the effective plastic strain, $\bar{\dot{\varepsilon}}_p$ is a dimensionless effective strain rate with $\bar{\dot{\varepsilon}}_p = \dot{\varepsilon}_p/\dot{\varepsilon}_0$ where $\dot{\varepsilon}_0$ is the reference strain rate used in underlying material tests. $\bar{T} = (T - T_0)/(T_M - T_0)$ with T_0 being the initial temperature of the material during testing. T_M is the material's melting temperature, T the current temperature. In the model, two material failure criteria combined with the FE erosion method were used: the Cockcroft-Latham criteria [29] as well as a temperature limit, assuming a strength limit at 90% of the material's melting temperature.

Lead core material behavior was represented by the Steinberg-Lund constitutive model [30] where the shear modulus *G* and the yield strength σ_y are given by

$$G = G_0\left[1 + G_p'/G_0\, pV^{\frac{1}{3}} + G_T'/G_0\left(\frac{E_i - E_c}{R'} - 300\right)\right] e^{-\frac{fE_i}{E_m - E_i}}, \tag{2}$$

$$\sigma_y = \sigma_0[1 + \beta(\gamma_i + \bar{\varepsilon}_p)]^n\left[1 + b'pV^{\frac{1}{3}} + G_T'/G_0\left(\frac{E_i - E_c}{R'} - 300\right)\right] e^{-\frac{fE_i}{E_m - E_i}}. \tag{3}$$

The volumetric pressure response was represented by the Mie-Gruneisen EOS,

$$p = \frac{C^2\rho_0\mu[1 + (1 - \gamma_0/2)\mu - b/2\mu^2]}{[1 - (S_1 - 1)\mu - S_2\mu^2/(\mu+1) - S_3\mu^3/(\mu+1)^2]^2} + (\gamma_0 + b\mu)E. \tag{4}$$

In Eqs.(2,3) G_p'/G_0 and G_T'/G_0 represent pressure and temperature dependence on the shear modulus and are, together with the initial shear modulus G_0 and *f*, experimentally determined

constants. σ_0 is the initial yield stress, $b' = \sigma'_p/\sigma_0 \approx G'_p/G_0$ where σ'_p is the partial differential of σ_y with respect to pressure. $V = v_0/v$ is the relative volume with v_0 and v being the initial and the specific volume, respectively; p is the pressure and β and n are work-hardening parameters. E_i, E_m and E_c are the internal, melting, and cold compression energy per unit volume, respectively. R' is defined as $R' = R\rho/A$ with R being the gas constant and A the atomic weight, $\gamma_i$and $\bar{\varepsilon}_p$ are the initial and equivalent plastic strain, respectively. In Eq.(4), E is the internal energy, γ_0 is the Gruneisen coefficient with b the volume correction to γ_0. C is the bulk sound speed. S_1, S_2, S_3 are the Hugoniot slope coefficients and $\mu = \rho/\rho_0 - 1$ is the compression coefficient.

Employed material parameters were adopted from the literature [31-35] and listed in Tables 1-5.

Table 1. Bullet jacket material constants for Johnson-Cook model (A, B and W_{cr} in MPa; T, T_m in K; $\dot{\varepsilon}_0$ in s^{-1})

Material	A	B	n	$\dot{\varepsilon}_0$	C	T	T_m	m	W_c	D_c	β
90/10 Brass	206	505	0.42	5.0E-04	0.01	293	1189	1.68	914	1.0	0.0

Table 2. Bullet lead core material constants for the Steinberg model

Material	$b' \approx G'_p/G_0$ [mm²/N]	G'_T/G_0 [K^{-1}]	R' [$NK^{-1}mm^{-2}$]	β	n	γ_0	f	a
Lead	11.63E-05	1.16E-03	0.455	110	0.52	2.74	0	2.2

Table 3. Bullet jacket material properties

Material	ρ [t/mm³]	E [MPa]	v	C_p [J/tK]	α [K^{-1}]
90/10 Brass	8.95E-09	123.0E03	0.3	418.0E06	1.9E-05

Table 4. Bullet lead core material properties

Material	ρ [t/mm³]	G_0 [MPa]	σ_0 [MPa]	σ_{max} [MPa]	T_{m0} [K]	A [t/mol]
Lead	11.34E-09	8600	8	100	760	207.2E-06

Table 5. Mie-Gruneisen EOS parameters for lead material

Material	C_0 [mm/s]	S_1 [-]	S_2 [-]	S_3 [-]	γ_0[-]	b[-]
Lead	2.0E-06	1.429	0.8506	-1.64	2.74	0.54

During high-speed impact severe deformation/fragmentation of the bullet may occur. To avoid drawbacks of standard Lagrangian elements under extreme distortion, bullets, Figs.5a,b, were modeled using smoothed-particle hydrodynamics (SPH) elements with a renormalized

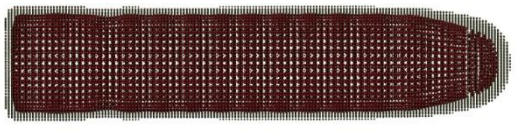

Fig.5a Bullet model: SPH elements used for jacket and core representation (section cut view)

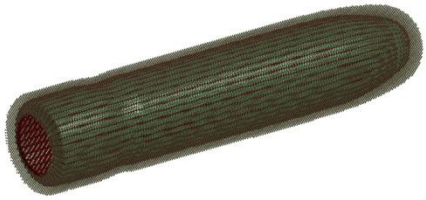

Fig.5b Bullet model: uncut (perspective view)

Lagrangian formulation, to account for excessive deformation during bone/brain contact. Since bullet jacket and core materials are only loosely connected, a penalty-based contact was defined between both constituents.

3.2 Head model

Based on digitalized CT-scan data the head model includes: scalp skin, cortical bone, cancellous bone, CSF, and brain, Figs.6a-c.

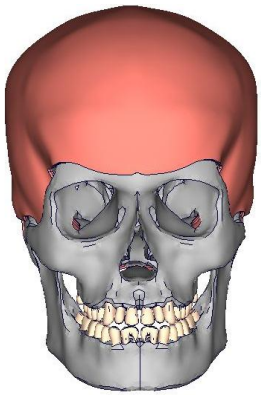

Fig.6a FE head model

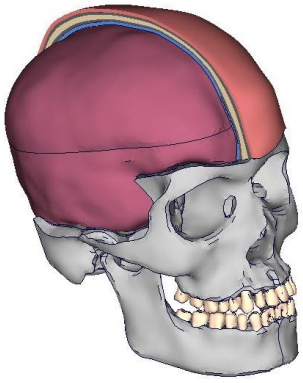

Fig.6b Section cut view: scalp skin, cranial bone, CSF, brain (from exterior to interior)

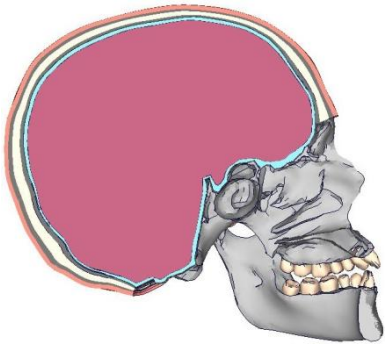

Fig.6c Side section cut view

3.2.1 Scalp skin

Scalp skin was included since, in general, skin stiffens significantly at increasing loading rates [36,37]. Experimental human skin data collected under tension at a strain rate of 167 s^{-1} was used for tissue representation [37]. The isotropic Ogden form was employed to define tissue behavior [38,39], skin anisotropy was neglected. An algorithm based on the simplex strategy was used to optimize model parameters constraining Poisson's ratio to $\nu = 0.497$. Employed values are shown in Table 6. Effective failure strain was estimated at 0.25, based on strain at peak stress [37]. Scalp skin tissue was modeled using thick shell elements with two elements over the thickness. Skin thickness was assumed to average 6.5 mm [40,41].

Table 6. Parameters for scalp skin tissue

μ_1 [MPa]	μ_2 [MPa]	α_1 [-]	α_2 [-]
0.30279	0.12096	21.26804	0.40587

3.2.2 Skull bone

Data used in this report for human cortical and cancellous bone were adopted [42-56]. In contrast to dry bone, wet bone can pass through a plastic phase [57]. Thus, a rate-dependent elasto-plastic material model with plastic strain to failure criteria was used, based on both tension and compression yield stress versus effective plastic strain. Failure strain was estimated based on findings for cranial cortical bone and for femoral cortical bone [45,56]. A factor of 1.4 between the response in mechanical strength to tension and compression of

cancellous bone was deduced [58,59] as well as for cortical bone [60,61]. Employed bone material data is shown in Table 7, including Young's modulus for tension/ compression, E_t/E_c, Poisson's ratio ν, yield stress during tension/compression $\sigma_{y,t}/\sigma_{y,c}$, and plastic failure strain during tension/compression, $\varepsilon^f_{p,t}/\varepsilon^f_{p,c}$ (assumed equal).

Table 7. Employed wet bone material constants for $\dot{\varepsilon} = 10^5 - 10^6\ s^{-1}$ (σ in MPa)

Material	ρ [t/mm³]	E_t [MPa]	E_c [MPa]	ν	$\sigma_{y,t}$	$\sigma_{y,c}$	$\varepsilon^f_{p,t} = \varepsilon^f_{p,c}$
Cortical	1.9E-09	26000	36000	0.22	36	68	0.0075
Cancellous	1.7E-09	10200	7300	0.10	28	21	0.0055

Volumetric densities were adopted from Sharma and Fry et al. [62,63]. Cranial suture structures were not included in the model since findings are mixed regarding suture strength in adults compared to adjacent bone [64-66]. Stacked thick shell elements with two elements over the thickness were used to model cortical and cancellous bone layers.

3.2.3. Cerebrospinal fluid

CSF was considered a Newtonian fluid with properties close to water. It was modeled with tetrahedral continuum elements employing zero-stiffness material definition in addition to a linear polynomial EOS to accommodate for high-pressure shock loading. Coefficients were C_1 = 2190 MPa, C_2 = 9224 MPa and C_3 = 8767 MPa fitting Hugoniot data for water [67-70]. The subarachnoid space was set to a constant thickness of 2 mm. A penalty contact between outer and inner CSF surface to inner skull bone and outer brain surface was assigned. A dynamic shear viscosity coefficient of μ = 3.5E-09 [MPa·s] was used.

3.2.4 Brain tissue

Based on the similarities of human and porcine brain tissue, porcine brain is often used for testing. Based on tests with varying strain rate in porcine brain tissue samples during compression ($\leq 90\ s^{-1}$), shear ($\leq 120\ s^{-1}$) and tension ($\leq 90\ s^{-1}$) instantaneous shear moduli in the range of 12-27 kPa were deduced [71-75]. Similarly, based on tests including porcine brain at shear rates up to $800\ s^{-1}$, a mean instantaneous shear modulus of 14 kPa was derived [76]. Shear tests on bovine brain tissue at a shear strain rate of $700\ s^{-1}$ led to an instantaneous shear modulus of 54 kPa [77]. In this report, a viscoelastic Maxwell model was used to describe brain tissue mechanical properties:

$$G(t) = \sum_{i=1}^{n} G_i \exp\left(-\beta_i t\right). \quad (5)$$

The deviatoric response was modeled based on experimental data of white matter tested in shear up to 6300 Hz [72]. From this data, instantaneous and long-term shear moduli of 62 kPa

and 0.27 kPa, respectively, can be deduced. Employed Prony series shear relaxation moduli and shear decay constants are provided in Table 8.

Table 8. Employed brain material parameters

i	1	2	3	4	5	∞
G_i [kPa]	50.0	6.22	2.49	1.23	1.62	0.27
β_i [s^{-1}]	1.0E+05	4350.0	200.0	5.3	0.0051	1.0E-25

Brain tissue was assumed isotropic and modeled with under-integrated constant stress hexahedral continuum elements with hourglass stabilization. The element erosion method was defined to account for material failure, assuming principal failure strain to be in the range of 40% [79]. To conserve mass and momentum, Lagrangian solid elements used for brain modeling and exceeding the failure strain were eroded from the mesh and defined to transform to freely-moving SPH particles. These in turn were set in contact definition to adjacent Lagrangian elements of brain and skull to continue their contribution to the fragmentation process.

4 Forensic evidence

4.1 Bullet fragments

Following the assassination, three small bullet lead fragments and two larger jacket fragments, Figs.7,8, were found in the limousine (exhibits CE567 and CE569, [5]).

Fig.7a Exhibit CE569

Fig.7b Exhibit CE569

Fig.8a Exhibit CE567

Fig.8b Exhibit CE567

Credit: National Archives and Records Administration

Figs.7a,b show different views of the base of one fragment. Figs.8a,b show parts of a jacket fragment with core lead material from different views. Whether both fragments were components of the same bullet could not be determined [12].

Fragments CE569 (Figs.7a,b) and CE567 (Figs.8a,b) exhibit unique features that were used for comparison with simulation results. From fragment CE569 it is evident that

- the lead core separated from the jacket base, Fig.7a
- the jacket is folded (flapped) back on one side, several millimeters above the cannelure, Fig.7b, while the opposite side is torn down to just above the cannelure, Fig.7a
- the base is flattened (elliptic cylinder) and indented on one side, Fig.7b

From fragment CE567 it is evident that

- the surface of the bearing jacket is irregularly bent open
- the jacket surface is cracked and torn open in the middle (visible lead material), Fig.8a
- the core lead material is strongly deformed (mechanically and heat based), Fig.8b

4.2 Autopsy X-rays of Kennedys' head

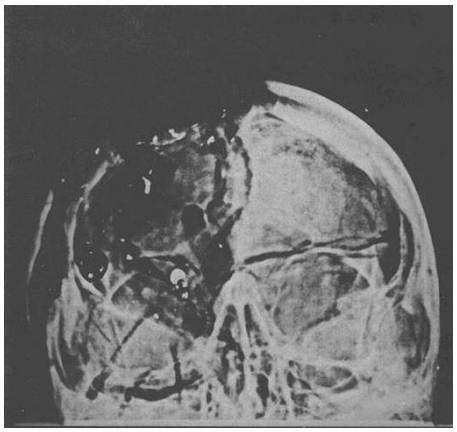

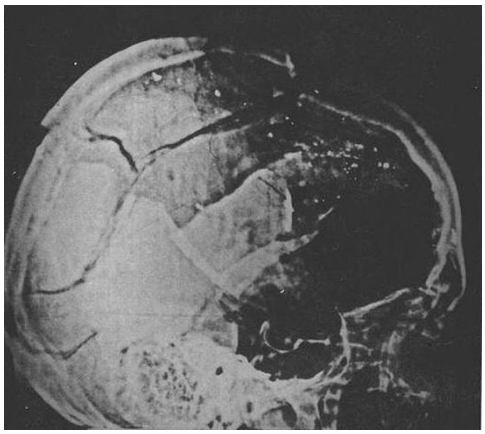

Fig.9a Front head anterior-posterior X-ray **Fig.9b** Lateral right side X-ray
Credit: National Archives and Records Administration

The skull X-ray photographs of JFK [5,12] have been variably interpreted, including possible alteration [81,82]. The HSCA photographic panel, however, unanimously agreed that all X-rays (and autopsy) photographs had not been altered in any manner [12]. Computer enhanced versions of the original X-ray photographs are shown in Figs.9a,b, as has been shown in the HSCA report [12]. They show that the top right side of the skull is extensively damaged with extreme loss of bone (Fig.9a) and multiple fracture lines (Fig.9b), [77].

4.3 Autopsy photographic evidence

In this report the following images were partly masked, due to their graphic content. Autopsy photographs Figs.10a,b show Kennedy's head and face from both sides. In Fig.10a, a large defect in the temple region of the right frontal bone resembling a sharply demarcated 'V' is apparent. No damage is visible to the left side of the head, Fig.10b. The autopsy photograph Fig.10c shows a circular wound indicated with {E} (cf. also [6] and exhibit F-48 in [12]), identified as the bullet entrance site by the HSCA.

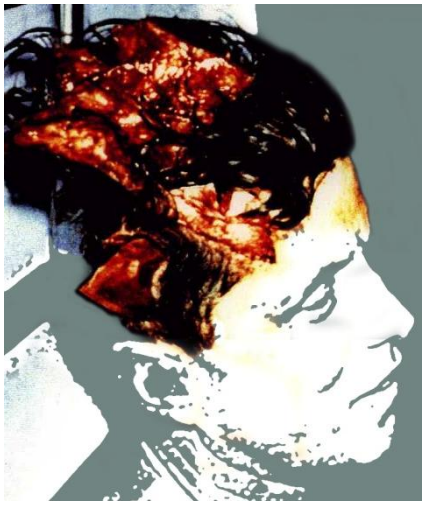

Fig.10a Autopsy photos: V-shaped trauma in the right temple region

Fig.10b Left side view

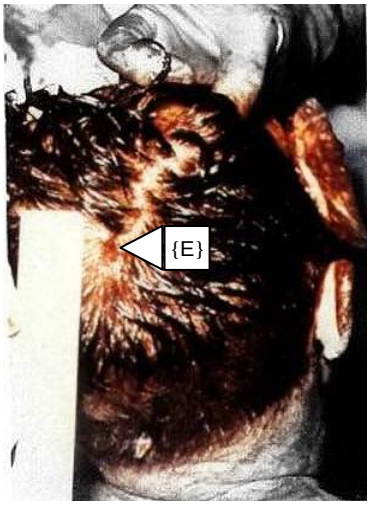

Fig.10c Top rear view: bullet entrance site [12] - indicated with {E}

Credits: US-Government/Wikimedia/Commons/Public Domain and JFK Lancer

5 Results

Based on the conditions described in section 2.1 shots were simulated from four directions: 1. from behind originating from the Texas School Book Depository, 2. from the right, the Grassy Knoll, 3. from the front/slight left - the South Knoll and 4. a storm drain in the slight right front. Simulated bullet and bone fracture characteristics resulting from these directions are compared with forensic evidence. The simulation results based on the shot direction concluded by the *Warren Commission*, i.e. from the TSBD, are presented first (analysis in full detail) followed by the results of the three other shot directions.

Numerical simulations were conducted using the LS-DYNA (Livermore Software Technology Corporation, USA) explicit hydrocode.

(Note: reported simulation times always refer to time Δt after initial bullet-head contact)

5.1 Simulated shot from the TSBD-direction

Official information of the HSCA and Clark reports differ regarding the horizontal orientation of the bullet wound to the back of JFK's head (cf. Section 2.2). An intermediate value of 21.5 mm was set as the distance from the head midline in the present investigation. In advance, due to the uncertainty of the horizontal impact location, a sensitivity analysis was conducted varying the impact site by ±3 mm around the intermediate value in steps of 1 mm to investigate whether the bone crack propagation and bullet jacket fragmentation might change. Varying the impact site in this way resulted only in minor deviations to the shape of the fragmented skull bone and bullet geometries, indicating a robustness of the results. Simulation results (at time t = 0.85 ms) are depicted in Figs.11a-c, correlating evidence is

shown in Figs.11d,e. In this investigation, only bullet jacket deformation was compared since lead core material deformation was unspecific in geometry.

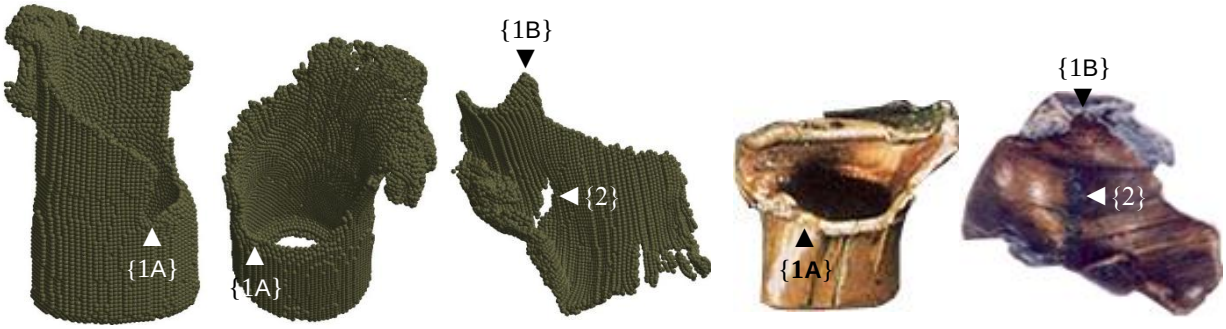

Fig.11a Jacket fragmentation **Fig.11b** Top view of Fig.11a **Fig.11c** Fragment torn off of the jacket surface **Fig.11d** Ex. CE569 **Fig.11e** Ex. CE567

The simulation showed that a large portion of the jacket surface, Fig.11c, tore off the base at position {1A}, Figs.11a,b, to finally separate from it. Positions {1A} and {1B} were initially identical before separation. Further, the simulated jacket surface was cracked and torn open in the middle section at location {2}. Correlating positions in the evidence fragments are indicated. Also similar to the evidence, the jacket was flapped back on one side while the opposite side was torn down to above the cannelure, Figs.11a,b, and the base was deformed to an elliptic shape (note that proportions of Figs.11a-c and Figs.11d,e do not correspond). This agreement thus shows that both fragments were very likely components of the same bullet, an argument which has been raised in section 4.1 [12]. From the simulation process, different stages can be distinguished.

1: Initial contact with the skull bone, damaging the bullet's nose with the jacket tearing open to expose the lead core. The initially stable single cell one-end closed tube structure then assumes the shape of a fragile two-end open tube structure. Bullet entrance is indicated with {1} in Fig.12a.

2: Contact with brain tissue. Here partial asymmetric mushrooming of the jacket occurrs due to asymmetrical initial bone contact (impact angle not orthogonal to bone surface) and partial disconnection of the lead core from the jacket. Disconnection was driven by faster forward movement of the lead core caused by higher contact forces (due to locking and friction) on the jacket by adjacent tissue. Due to asymmetric bullet deformation and resulting asymmetric resistance bullet rotation begins around the vertical z-axis (s. Figs.13 for coordinate system). This caused indentation of the jacket base since the lead core had already traversed forward leaving the jacket base hollow.

3: Second contact with bone as the bullet exits, indicated with {2} in Fig.12a in the right temple region, and shown in detail in Fig.12b. At exit the bullet was rotated approximately 35° about the vertical z-axis compared to its pre-impact line of flight. Here progressive damage to the jacket and core occurs (again asymmetrically, due to unilateral contact to the parietal/frontal bone structure).

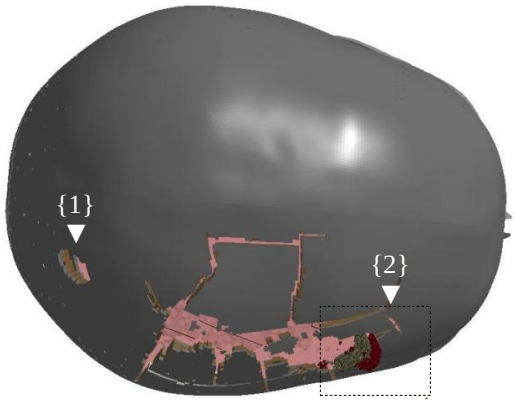

Fig.12a Bone damage at t = 0.3 ms; entrance wound at {1}, bullet exit site at right temple {2}

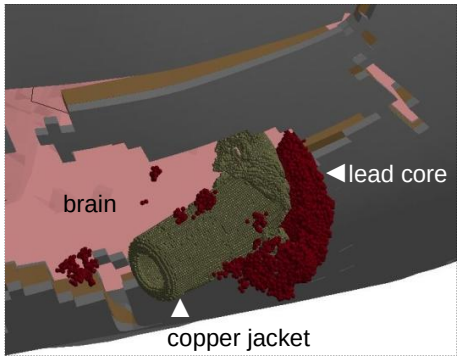

Fig.12b Detail from Fig.12a: bullet position and damage at time of exit

4: Post-impact phase (t > 0.3 ms). Due to centrifugal forces on the bullet material, further deformation and rupture of the jacket material occurred until the lead core base completely separated from the jacket (after exit, the bullet was free of external forces previously exerted by brain tissue and bone). Simulation showed that exiting fragments had an average resultant velocity of 350 m/s. Forensic evidence suggests that after exit, fragments of the fatal bullet contacted the car interior [1].

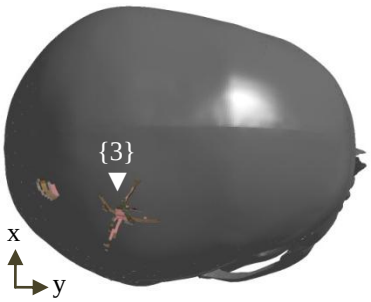

Fig.13a Bone damage initiating at time t = 0.14 ms

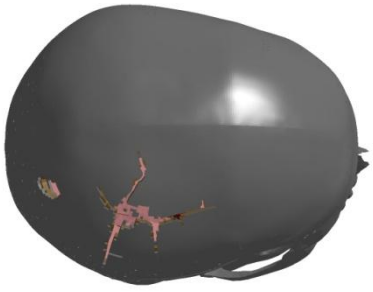

Fig.13b Time t = 0.18 ms

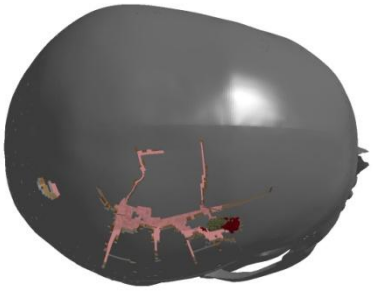

Fig.13c Time t = 0.25 ms

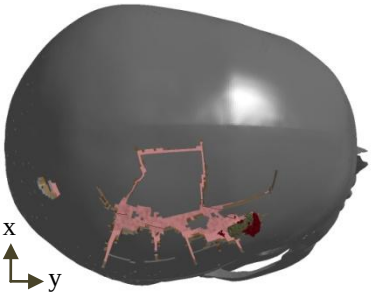

Fig.13d Time t = 0.28 ms

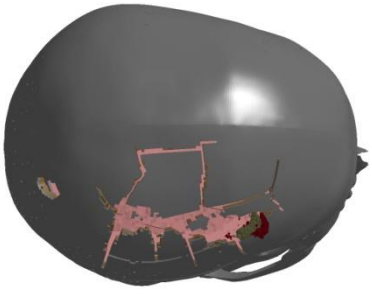

Fig.13e Time t = 0.29 ms

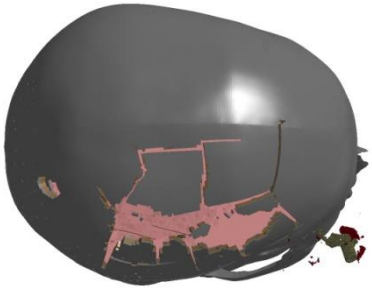

Fig.13f Time t = 0.4 ms

Very likely, this led to further bullet deformation, however, of unknown degree. Such additional deformation might be a source of inaccuracy between the deformation resulting from the simulations presented here, i.e. only bullet-head contact was considered, and the recovered fragments.

Besides the two large deformed jacket fragments, in the simulation the soft lead core also exhibited intense deformation and fragmentation and separated into multiple small fragments during and after brain penetration. In Figs.13a-f simulated progressive damage to the skull is shown (scalp skin, CSF and adaptive SPH brain elements are masked for better visibility). Due to the high location of bullet entrance and motion direction, the bullet travels closely beneath the inner cortical bone layer. This results in local increase of intracranial pressure which initially cracks the skull open in the right parietal rear of the head (position {3} in Fig.13a) and fracture lines, beginning around the site of the crack origin, radiate concentrically, Fig.13a. As the maximum intracranial pressure location propagates along with the bullet towards the exit site, more fracture lines radiate off orthogonal to the emerging fracture path, Figs.13b-e.

Plates of bone between these fracture lines are bent outwards, Figs.14a,b. Similar crack propagation in bone has been reported [84]. Figs.14a,b depict the damage to the head (at times t = 0.8 ms and 0.85 ms, respectively) with the scalp skin and adaptive SPH brain elements shown. The V-shaped demarcation defect (localized with {1} and {2} in Fig.14b) is clearly apparent in the simulation results. The straight, sharp fracture line can be seen more clearly in

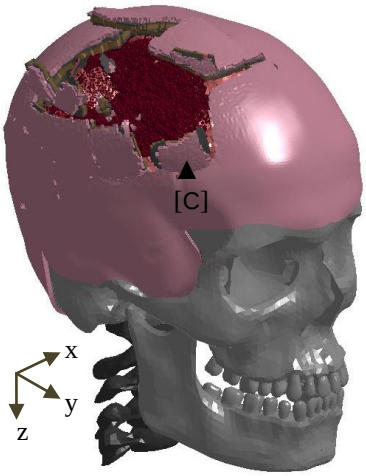

Fig.14a Model: skull and scalp skin damage at time t = 0.8 ms

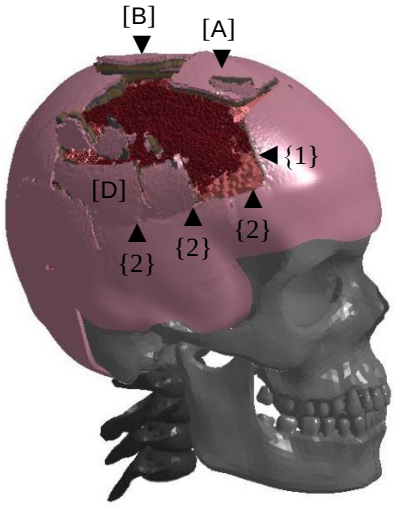

Fig.14b Model: skull and scalp skin damage at t = 0.85 ms (fragment [C] has separated and is not shown)

Fig.14c Autopsy photograph (identical to Fig.10a)

Fig.15a. The correlating positions in the evidence are indicated in Fig.14c. In Figs.14a,b bone fragments [A-C] separated from the skull in the course of the simulation and moved with an

average vertical z-velocity of -16, -25 and 7 m/s, respectively, indicated by to the coordinate system shown in Fig.14a, and their lateral (x-) and forward (y-) velocity components were 7, 10, -23 m/s and 3.5, -1, 37 m/s. The masses of the bone fragments [A-C] were 23, 25, and 15g, respectively. Separation of fragments [A,B] from the skull drive them vertically away from the initial crack zone, rotating at the same time around the scalp skin connection located approximately at the sagittal suture, until total skin rupture occurs. Fragment [D] in Fig.14b behaves similarly in the right lateral direction, rotating about the scalp skin connection along fracture path {2}. Its mass is 35 g. Average vertical z-velocity of fragment [D] is -1.3 m/s, its lateral x- and forward y-velocity components are -28 m/s and 10 m/s, respectively. Fragment [B] is parietal bone. Parietal/ frontal bone fragment [A] slightly extends over the coronal suture. Analysis regarding a possible match of the fragments [A-D] with the fragments recovered from the scene of the assassination ([5], exhibit CE387) was not further pursued.

The image shown in Fig.15b is an enhanced copy of the fractures shown by X-ray (unenhanced X-ray images are presented in the HSCA report [12]) and can be compared to

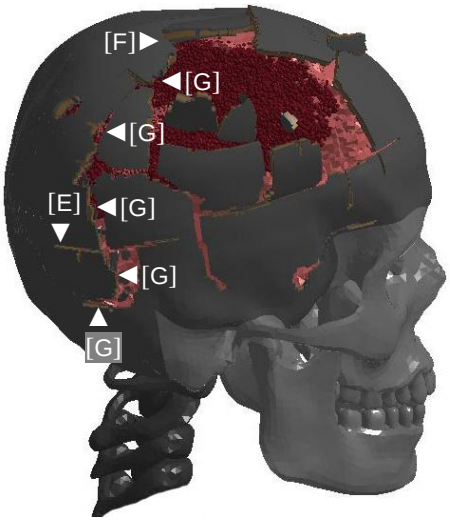

Fig.15a Underlying skull bone damage (scalp skin masked) at t = 0.85 ms

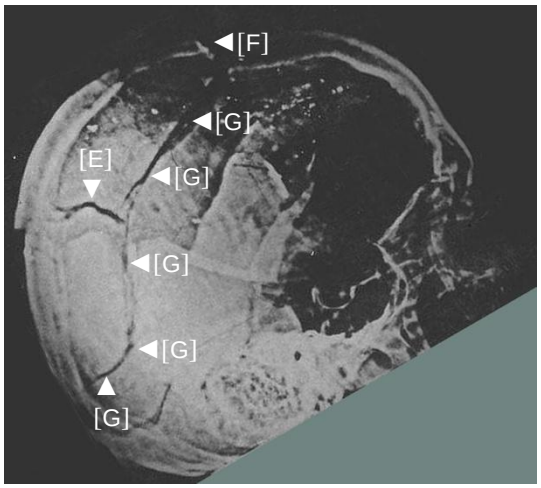

Fig.15b Lateral right side X-ray: fracture lines (analog to Fig.9b but rotated for comparison) (Credit: National Archives and Records Administration)

the simulation model Fig.15a, although exact perspectives differ. Descriptions of single fracture lines of the HSCA radiologists can be found in exhibits F-32,33 [12]. The distinct S-shape along line [G] in Fig.15b correlates with the path in Fig.15a. Similarly, [E] coincides, and [F] indicates the rearmost fracture line of fragment [B] in Fig.14b. The front head X-ray, Fig.9a, shows that skull damage extended to the sagittal suture. This is also seen in the simulation results in Fig.13f and Figs.14a,b. It becomes apparent from figures Figs.14a,b and Fig.15a that to a large extent the scalp covered underlying bone damage. Extensive underlying

bone damage coincides with the testimony of one of the autopsy pathologists stating that during the autopsy the skull was all "*falling apart*" [85]. The wound characteristics visible from the outside, cf. Fig.14a, could well correlate with the wound location reported by eyewitnesses [6,8] as it largely extends to the right back of the head.

5.2 Simulated shot from the GK-direction

Skull fractures and bullet fragmentation resulting from a simulated shot from the *GK*-direction are shown in Figs.16a-d. The bullet impact site indicated with {1} was chosen to be at the right temple region in close proximity to where the sharp bone defect is apparent in the autopsy images, cf. Figs.1,2 for geometrical orientation. The resulting exit site is indicated with {2} with the arrow indicating the bullet orientation prior to contact. Simulation shows that bone fracture lines and bullet deformation do not resemble the evidence, Figs.7-9a,b. A shot from the *GK*-direction would have inevitably led to a bullet exit site directly opposite the entrance site, i.e. the left temple region (evidently in contradiction to Fig.10b) and not as hypothesized by some [6,8] at the right rear of the head.

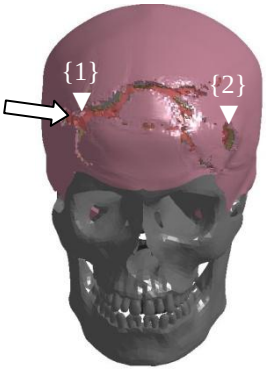

Fig.16a Scalp skin and bone damage at t = 0.85 ms (arrow indicates shot direction)

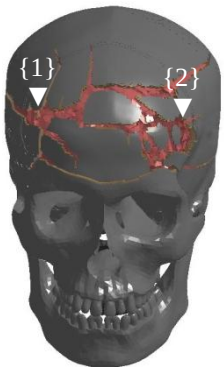

Fig.16b Bone damage at t = 0.85 ms

Fig.16c Jacket fragmentation at 0.55 ms after exit

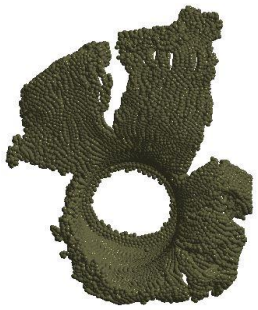

Fig.16d Jacket fragmentation at 0.55 ms after exit (top view)

5.3 Simulated shot from the SD-direction

The skull fractures and bullet fragmentation resulting from a simulated shot from a storm drain situated almost in front of the limousine are shown in Figs.17a-d.

The bullet impact site was set at the right temple indicated with {1} in Figs.17a,b. The exit site is indicated with {2}. The arrow indicates bullet orientation prior to contact. Simulation shows that bone fracture lines and bullet deformation do not resemble the evidence. Jacket deformation shows expansion and folding back as well as indention at the base. In the course of penetration and specifically after exit, the lead core, however, does not tear the bullet jacket to initiate separation of the jacket into another larger piece. Ejected bone fragments are also

not apparent. In addition, the V-shaped defect in the right temple is absent. The bullet exit site is indicated with {2} in the lower left area at the back of the head, Fig.17c.

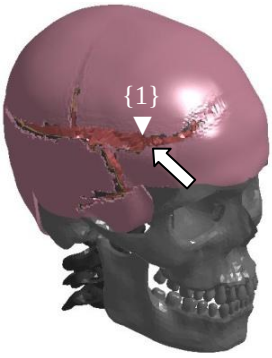

Fig.17a Scalp skin damage at t = 0.85 ms (arrow indicates shot direction)

Fig.17b Bone damage at t = 0.85 ms

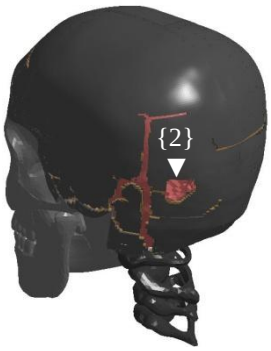

Fig.17c Bone damage at t = 0.85 ms (rear view)

Fig.17d Jacket fragmentation at 0.55 ms after exit

5.4 Simulated shots *from the SK-direction*

Three possible shooter origins, cf. Fig.1, were analyzed. Common to all sites is an assumed entrance site over the right supra-orbital ridge {1} resulting in an exit site at the right rear of the head, {2} in Fig.18a.

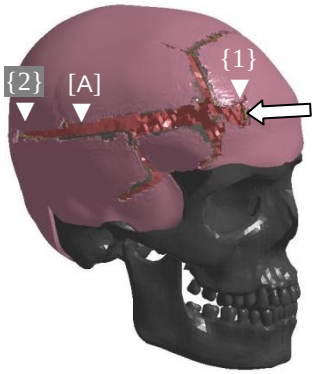

Fig.18a Shot from site (3): scalp skin damage at t = 0.85 ms (arrow: shot direction)

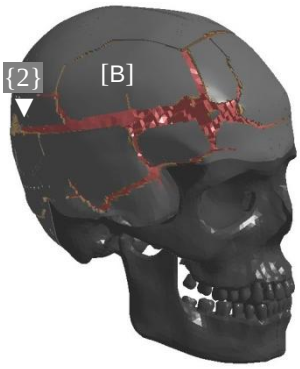

Fig.18b Bone damage at t = 0.85 ms

Fig.18c Jacket fragmentation at 0.55ms after exit

Fig.18d Jacket fragmentation (opposite perspective)

Bullet entrance sites further lateral left of {1} were considered geometrically unlikely due to Mrs. Kennedy's position at the time of the fatal shot shielding Kennedys' left head side, cf. Fig.3a,b. Potential shot origins (1) and (2), Fig.1, are approximately in line (from a vertical point of view) with the shot trajectory from the TSBD. Simulation showed that skull fractures and bullet fragmentation were similar for all three cases; bullet exit sites differed slightly. While for locations (1) and (2) the bullet exit site was located at the right rear of the head, for location (3) it was a further to the right. For all three cases a distinct bullet entrance opening can be detected at {1}, which is not evident in the autopsy image Fig.10a. Further, bullet jacket deformation and fragmentation, Figs.18c,d, do not resemble the evidence.

5.5 Simulated post-impact phase: head and upper body motion

Immediately after the head shot, a violent back- and leftward motion of the JFK's head and upper body is apparent, cf. *Zapruder Film* frames #316-320 [10]. This caused controversy about the shot direction since the lay community expects a body to be driven in the same direction as the pre-impact direction of a bullet that impacts it, not in the opposite direction. It could however clearly be shown by simulation employing the presented head model coupled with a dummy model [86] that retrograde motion is of mechanical cause and based on conservation of momentum. Momentum exchange of expelled bone, parts [A-C] in Fig.14a,b, as well as brain matter drives the head into retrograde motion and not forward. This was first proposed in 1976 [87], recently confirmed by Nalli [88]. Simulation shows that 50 g of brain FE-elements fail as a result of a shot from the TSBD of which approximately 25 g had an average velocity of 25 m/s that contributed to momentum exchange. With velocity components, Fig.19a, and masses, section 5.1, the average resultant velocity of the head was deduced to be 0.53 m/s in agreement with the literature [89].

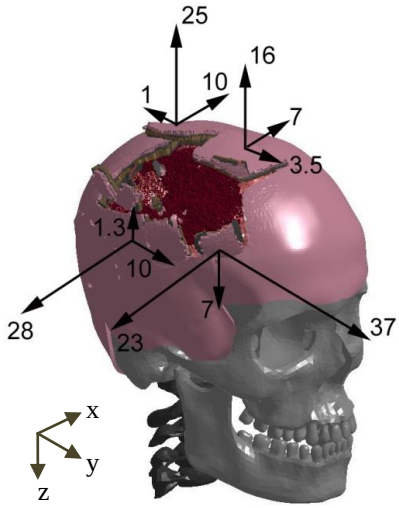

Fig.19a Velocity components [m/s] of main skull fragments at t = 0.8 ms

Fig.19b t = 0.85 ms (expelled bone/ brain was not included)

Fig.19c t = 330.85 ms (red lines indicate arm trajectories)

Simulation showed that transferred momentum initially leads to a head rotation around the vertical (z-) axis and, synchronously, a lateral flexion about the in-sight (y-) axis until finally being decelerated and stopped relative to the upper body by the physiologic rotation limits of the neck joints. Approaching these limits, simulation further showed that the upper body was also accelerated to rotate around the pivot at the pelvis and the lumbar vertebrae, Figs.19b,c.

6 Discussion

Due to controversy surrounding official reports in regard to the assassination of John F. Kennedy, the fatal head shot was analyzed in the present report by means of numerical

simulation and outcome of different simulated shot directions were compared to forensic evidence. Shot directions included the officially designated shot origin site from the Texas School Book Depository to the back of the president's head, as well as three additional sites promoted by conspiracy theories. It was postulated that the specific characteristics and complexity of anatomic and physical evidence existent in the form of X-ray and autopsy photographs as well as recovered bullet fragments and post-impact head motion can be reproduced by simulation from only one shot direction. Specifically, unique features were the sharply demarcated defect in the temple region of the right frontal bone, evident in autopsy photographs, as well as the specific skull bone crack formation evident in X-rays. Deformation of the bullet jacket material was also particularly characteristic. Comparing all simulation results with the evidence, it could be shown that only a bullet fired from a direction in Kennedy's rear, specifically originating from the direction of the Texas School Book Depository at a ground height approximately matching the 6th floor correlates well with the evidence. The sharply demarcated V-shaped defect in the temple region of the right frontal bone, which at first glance appears artificial and had been proposed as the result of manipulation to cover a wound resulting from a shot from the front [81], was shown to be a direct consequence of the particular loading situation. For all simulated cases it is shown that though the bullet deforms, fractures, and rotates, it generally follows a straight path in the soft brain tissue, such that the exit site is in line with the pre-impact bullet flight path. This rigorously excludes hypotheses including locations other than the TSBD as shot origin, cf. shot traces in Fig.2 as they contradict autopsy evidence, Figs.10b,c.

7 Conclusions

The presented simulations support the official commission reports regarding origin and direction of the fatal head shot to John F. Kennedy. From a mechanical standpoint, based on computational simulation, JFK's head was hit by a single bullet from the rear originating from the Texas School Book Depository. Deformation patterns regarding skull fracture and bullet jacket deformation as shown in photographs could be matched by simulation with unambiguous consistency, leaving little room for further speculation about the origin of the projectile. Simulated post-impact head motion corresponds to evidence provided by the *Zapruder Film*. Simulation results together with forensic evidence exclude the sites "*Grassy Knoll*, *South Knoll*, and storm drain", as potential origins of the fatal shot.

The modeling approach employed here, based on computer-aided simulation, could be applied to similar cases in the forensic field.

Appendix

Simulated post-impact phase: bullet fragment traces resulting from a shot from the TSBD

Simulated traces (green lines) of the major bullet fragments are shown in Figs.20a,b (to enhance visibility, the right door side and the seat in front of Kennedy are masked). All traces at time $t > 0.85$ ms were linearly extrapolated from the simulated trace results at $t = 0.85$ ms. Simulation shows that most fragments - including those depicted in Figs.11a,c - travelled towards the driver's seat. Smaller fragments of the bullet jacket material were deflected at head contact and moved towards the windshield frame and the windshield.

Even though simulated traces are approximations (they depend on initial projectile velocity, all material properties, initial head position, contact interactions and the impact wound location used in the model) they coincide with the fact that fragments were recovered from the left front of the presidential limousine, whereas others hit the windshield [1].

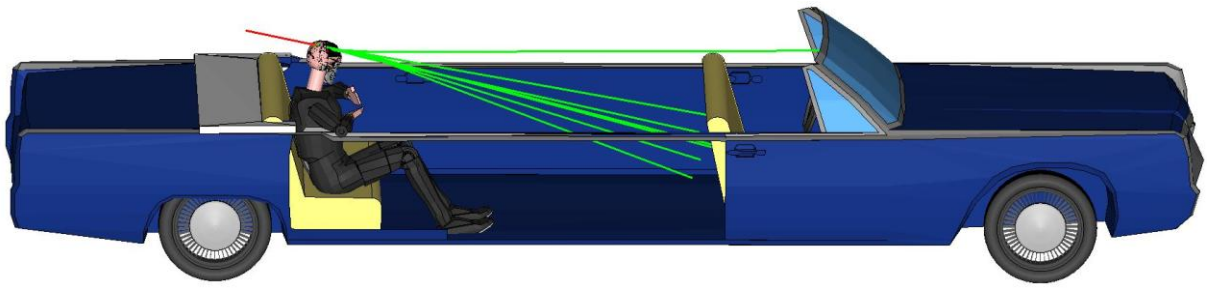

Fig.20a. Bullet pre-impact trace (red) and fragment post-impact traces (green) - (true scale model [5,12])

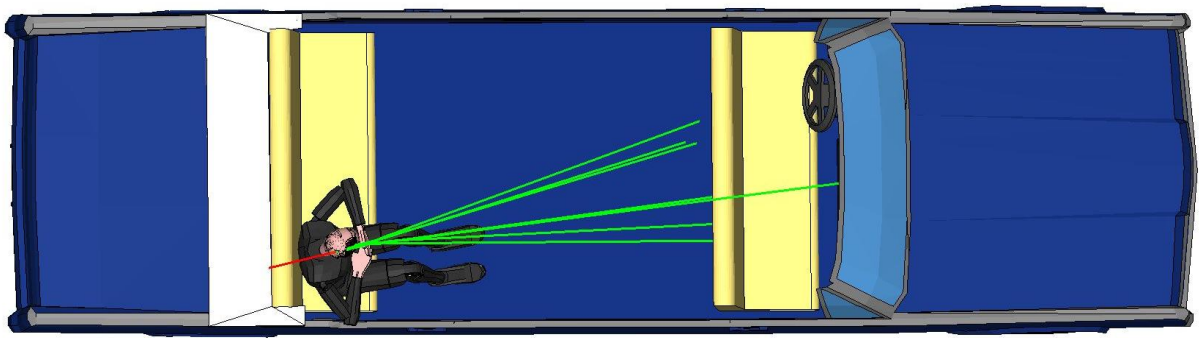

Fig.20b. Bullet pre-impact trace (red) and fragment post-impact traces (green) - top view

References

1. Warren E (1964) The President's Commission On The Assassination Of President Kennedy Hardcover, U.S. Government Printing Office
2. Hawks W (1963) White House transcript of the press conference at Parkland Memorial Hospital, Dallas, Texas, Nov.22
3. Smith M (1963) Cut down by a sniper in Dallas, New York World-Telegram and Sun
4. Wicker T (1963) Gov. Connally shot; Mrs. Kennedy safe, The New York Times
5. Warren Commission Report (1964) Report of the President's Commission on the Assassination of President Kennedy, United States Government Printing Office, Washington, DC
6. Groden R (1993) The Killing of a President, Penguin Books, NY
7. Crenshaw CA, Hansen J, Shaw JG (1992) JFK: A conspiracy of silence, Signet, NY
8. Aguilar GL (1994) John F. Kennedy's Fatal Wounds: The Witnesses and the Interpretations from 1963 to the Present, Issue 2, Electronic Assassinations Newsletter, http://assass-inationweb.com/ag6.htm
9. National Geographic (2013) JFK: The Final Hours, Documentary
10. Zapruder Family Collection 2018 (accessed 19 March 2018) The Sixth Floor Museum at Dealey Plaza, Dallas, TX; https://www.youtube.com/watch?v=TKcUL1EtbCI
11. United States House Select Committee on Assassinations 2018 (accessed 19 March 2018) https://en.wikipedia.org/wiki/United_States_House_Select_Committee_on_ Assassinations
12. HSCA (1979) Report of the Select Committee on Assassinations of the U.S. House of Representatives, United States Government Printing Office, Washington, DC
13. Horne DP (2009) Inside the Assassination Records Review Board: The U.S. Government's Final Attempt to Reconcile the Conflicting Medical Evidence in the Assassination of JFK, Vol. I-V, Douglas Horne
14. Garrison J (1988) On the Trail of the Assassins. Sheridan Square Press, New York
15. Lifton DS (1980) Best evidence: Disguise and Deception in the Assassination of John F. Kennedy. Macmillan Publishing Co., New York
16. Lane M (1966) Rush to judgement. Publisher: The Bodley Head, London
17. Buchanan TG (1964) Who killed Kennedy? G.P. Putnam's Sons, New York
18. Abramson J (2013) Kennedy, the Elusive President. New York Times, Oct.27, p. BR1

19. Drommer & Associates (1978) Topographic survey of a part of the northern portion of Dealey Plaza, Dallas, TX
20. Cutler R, Sprague RE (1970) Spatial chart of northern half of Dealey Plaza, Dallas, Texas, Prepared for: E.C. Berkeley Enterprises
21. Haag LC (2014) Tracking the Magic Bullet in the JFK Assassination, AFTE, 46 (2)
22. Haag LC (2014) President Kennedy's Fatal Head Wound and his Rearward Head Snap, AFTE, 46 (4)
23. Clark R (1968) Clark Panel Report: panel review of photographs, X-ray films, documents and other evidence pertaining to the fatal wounding of President John F. Kennedy, Assassination Records Review Board, MD 59
24. Mötz J (2001) Österreichische Militärpatronen - Austrian Military Cartridges, Vol. 2, Verlagsbuchhandlung Stöhr, Wien
25. Steinberg N (1994) Hatless Jack: the president, the fedora, and the history of an American style, Plume, Penguin Books, USA
26. Randich E, Grant PM (2006) Proper assessment of the JFK assassination bullet lead evidence from metallurgical and statistical perspectives, J Forensic Sci, 51 (4). https://doi.org/10.1111/j.1556-4029.2006.00165.x
27. Spiegelman C, Tobin WA, James WD, Sheather SJ, Wexler S, Roundhill DM (2007) Chemical and Forensic Analysis of JFK Assassination Bullet Lots: Is a Second Shooter Possible? Ann Appl Stat 1 (2). https://doi.org/10.1214/07-AOAS119
28. Camacho GT, Ortiz M (1997) Adaptive Lagrangian modeling of ballistic penetration of metallic targets, Comput Meth Appl Mech Eng, 142 (3-4). https://doi.org/10.1016/S0045-7825(96)01134-6
29. Cockcroft MG, Latham DJ (1968) Ductility and the workability of metals, Institute of Metals, 96
30. Steinberg DJ, Lund CM (1989) A Constitutive Model for Strain Rates from 10^{-4} to 10^{6} s^{-1}, J Appl Phys, 65 (4). https://doi.org/10.1063/1.342968
31. CIDEC (1970) Conseil International pour le Developpement du Cuivre, Geneve, data sheet No. D2
32. G.R. Johnson and W.H. Cook, A constitutive model and data for metals subjected to large strains, high strain rates and high temperatures, Proceedings of the 7th International Symposium on Ballistics, Den Haag, The Netherlands (1983).

33. Børvik T, Deya S, Clausen AH (2009) Perforation resistance of five different high-strength steel plates subjected to small-arms projectiles, Int J Impact Eng, 36. https://doi.org/10.1016/j.ijimpeng.2008.12.003
34. Steinberg DJ, Cochran SG, Guinan MW (1980) A Constitutive Model for Metals Applicable at High-Strain Rate, J Appl Phys, 51 (3). https://doi.org/10.1063/1.327799
35. Steinberg DJ (1996) Equation of State and Strength Properties of Selected Materials, Lawrence Livermore National Laboratory, Rept. UCRL-MA-106439
36. Lim J, Hong J, Chen WW, Weerasooriya T (2011) Mechanical Response of Pig Skin Under Dynamic Tensile Loading, Intl J Impact Eng, 38 (2). https://doi.org/10.1016/j.ijimpeng.2010.09.003
37. Otténio M, Tran D, Ní Annaidh A, Gilchrist MD, Bruyère K (2015) Strain rate and anisotropy effects on the tensile failure characteristics of human skin, J Mech Behav Biomed Mater, 41. https://doi.org/10.1016/j.jmbbm.2014.10.006
38. Ogden RW (1972) Large Deformation Isotropic Elasticity: On the Correlation of Theory and Experiment for Compressible Rubberlike Solids, Proc Roy Soc London-A, 328. https://doi.org/10.1098/rspa.1972.0096
39. Ogden RW (1984) Non-Linear Elastic Deformations, Ellis Horwood and John Wiley, Chichester. https://doi.org/10.1007/BF00047287
40. Parsons FG (1929) The thickness of the living scalp, J Anat, 63 (4)
41. Oldendorf WH, Lisaka Y (1969) Interference of scalp and skull with external measurements of brain isotope content: I. Isotope content of scalp and skull, J Nucl Med, 10
42. Evans FG, Lissner HR (1957) Tensile and Compressive Strength of Human Parietal Bone, J Appl Phys, 10. https://doi.org/10.1152/jappl.1957.10.3.493
43. Robbins DH, Wood JL (1969) Determination of Mechanical Properties of the Bones of the Skull, Expe Mech, 9 (5). https://doi.org/10.1007/BF02326542
44. McElhaney JH, Fogle JL, Melvin JW, Haynes RR, Roberts VL, Alem NM (1970) Mechanical Properties of Cranial Bone, J Biomech, 3. https://doi.org/10.1016/0021-9290(70)90059-x
45. Wood JL (1971) Dynamic Response of Human Cranial Bone, J Biomech, 4. https://doi.org/10.1016/0021-9290(71)90010-8
46. Carter DR, Hayes WC (1976) Bone Compressive Strength: the Influence of Density and Strain Rate, Science, 194. https://doi.org/10.1126/science.996549

47. Carter DR, Schwab GH, Spengler DM (1980) Tensile Fracture of Cancellous Bone, Acta Orthop Scand 51. https://doi.org/10.3109/17453678008990868
48. Røhl L, Larsen E, Linde F, Odgaard A, Jørgensen J (1991) Tensile and Compressive Properties of Cancellous Bone, J Biomech, 24 (12). https://doi.org/10.1016/0021-9290(91)90006-9
49. Kopperdahl DL, Keaveny TM (1998) Yield Strain Behavior of Trabecular Bone, J Biomech, 31 (7). https://doi.org/10.1016/S0021-9290(98)00057-8
50. Peterson J, Dechow PC (2002) Material Properties of the Inner and Outer Cortical Tables of the Human Parietal Bone, Anat Rec, 268 (1). https://doi.org/10.1002/ar.10131
51. Peterson J, Dechow PC (2003) Material Properties of the Human Cranial Vault and Zygoma, Anat Rec Part A, 274A. https://doi.org/10.1002/ar.a.10096
52. Kemper AR, McNally C, Kennedy EA, Manoogian SJ, Duma SM (2007) The Material Properties of Human Tibia Cortical Bone in Tension and Compression: Implications for the Tibia Index, Proceedings of the 20th Enhanced Safety of Vehicles Conference, Lyon, France, Paper Number: 07-0470
53. Motherway JA, Verschueren P, Van der Perre G, Vander Sloten J, Gilchrist MD (2009) The Mechanical Properties of Cranial Bone: the Effect of Loading Rate and Cranial Sampling Position, J Biomech, 42. https://doi.org/10.1016/j.jbiomech.2009.05.030
54. Sahoo D, Deck C, Yoganandan N, Willinger R (2014) Composite FE Human Skull Model Validation and Development of Skull Fracture Criteria, IRCOBI Conference, Berlin
55. Boruah S, Subit DL, Paskoff GR, Shender BS, Crandall JR, Salzar RS (2017) Influence of Bone Microstructure on the Mechanical Properties of Skull Cortical Bone - A Combined Experimental and Computational Approach, J Mech Behav Biomed Mater, 65. https://doi.org/10.1016/j.jmbbm.2016.09.041
56. Hansen U, Zioupos P, Simpson R, Currey JD, Hynd D (2008) The Effect of Strain Rate on the Mechanical Properties of Human Cortical Bone, J Biomech Eng 130 (1). https://doi.org/10.1115/1.2838032
57. Ong KL, Lovald S, Black J (2014) Orthopaedic Biomaterials in Research and Practice, Taylor & Francis, NY. https://doi.org/10.1201/b16369
58. Keaveny TM, Wachtel EF, Ford CM, Hayes WC (1994) Differences Between the Tensile and Compressive Strengths of Bovine Tibial Trabecular Bone Depend on Modulus, J Biomech, 27 (9). https://doi.org/10.1016/0021-9290(94)90054-x

59. Keaveny TM, Morgan EF, Niebur GL, Yeh OC (2001) Biomechanics of Trabecular Bone, Annu Rev Biomed Eng, 3. https://doi.org/10.1146/annurev.bioeng.3.1.307
60. Havaldar R, Pilli SC, Putti BB (2014) Insights into the Effects of Tensile and Compressive Loadings on Human Femur Bone, Adv Biomed Res, 3 (101). https://doi.org/10.4103/2277-9175.129375
61. Reilly DT, Burstein AH, Frankel VH (1974) The Elastic Modulus for Bone, J Biomech, 7 (3). https://doi.org/10.1016/0021-9290(74)90018-9
62. Sharma NK, Sharma S, Sehgal DK, Pandey RK (2014) Effect of Bone Composition and Apparent Density on Inhomogeneity in Energy Dissipation During Tension, Proc World Congr Eng 2014 Vol II, London
63. Fry FJ, Barger JE (1978) Acoustical Properties of Human Skull, J Acoust Soc Am, 63
64. Jaslow CR (1990) Mechanical Properties of Cranial Sutures, J Biomech, 23 (4). https://doi.org/10.1016/0021-9290(90)90059-c
65. Hubbard RP (1971) Flexure of Layered Cranial Bone, J Biomech, 4 (4). https://doi.org/10.1016/0021-9290(71)90031-5
66. Hubbard RP, Melvin JW, Barodawala IT (1971) Flexure of Cranial Sutures, J Biomech, 4 (6). https://doi.org/10.1016/0021-9290(71)90039-x
67. Rice MH, Walsh JM (1957) Equation of State of Water to 250 Kilobars, J Chem Phys, 26 (4). https://doi.org/10.1063/1.1743415
68. Walsh JM, Rice MH (1957) Dynamic Compression of Liquids from Measurements on Strong Shock Waves, J Chem Phys, 26 (4). https://doi.org/10.1063/1.1743414
69. Köster H, Franck EU (1969) Das spezifische Volumen des Wassers bei hohen drucken bis 600°C und 10 kbar, Berichte der Bunsengesellschaft für physikalische Chemie, 73, 716-722. https://doi.org/10.1002/bbpc.19690730717
70. Lysne PC (1970) A Comparison of Calculated and Measured Low Stress Hugoniots and Release Adiabats of Dry and Water Saturated Tuff, J Geophys Res, 75 (23). https://doi.org/10.1029/JB075i023p04375
71. Prange MT, Meaney DF, Margulies SS (2000) Defining Brain Mechanical Properties: Effects of Region, Direction and Species, Stapp Car Crash J, 44. https://doi.org/10.4271/2000-01-SC15
72. Nicolle S, Lounis SM, Willinger R (2004) Shear Properties of Brain Tissue over a Frequency Range Relevant for Automotive Impact Situations: New Experimental Results, Stapp Car Crash J, 48. https://doi.org/10.4271/2004-22-0011

73. Rashid B, Destrade M, Gilchrist MD (2012) Mechanical Characterization of Brain Tissue in Compression at Dynamic Strain Rates, J Mech Behav Biomed Mater, 10. https://doi.org/10.1016/j.jmbbm.2012.01.022
74. Rashid B, Destrade M, Gilchrist MD (2013) Mechanical Characterization of Brain Tissue in Simple Shear at Dynamic Strain Rates, J Mech Behav of Biomed Mater, 28. https://doi.org/10.1016/j.jmbbm.2013.07.017
75. Rashid B, Destrade M, Gilchrist MD (2014) Mechanical Characterization of Brain Tissue in Tension at Dynamic Strain Rates, J Mech Behav Biomed Mater, 33. https://doi.org/10.1016/j.jmbbm.2012.07.015
76. Shafieian M, Bao J, Darvish K (2011) Mechanical Properties of Brain Tissue in Strain Rates of Blast Injury, Bioengineering Conference (NEBEC) IEEE 37th Annual Northeast, Rensselaer Polytechnic Institute (RPI) in Troy, NY. https://doi.org/10.1109/NEBC.2011.5778711
77. Nie X, Sanborn B, Weerasooriya T, Chen W (2013) High-Rate Bulk and Shear Responses of Bovine Brain Tissue, Inter J Impact Eng, 53. https://doi.org/10.1016/j.ijimpeng.2012.07.012
78. Zhang W, Wu F, Feng L-l, Zhang R-r, Yu S-B, Wu C-w (2016) Differences in the Viscoelastic Features of White and Grey Matter in Tension, J Biomech, 49 (16). https://doi.org/10.1016/j.jbiomech.2016.10.032
79. Fiester (2012) Enemy of the Truth: Myths, Forensics and the Kennedy Assassination, JFK Lancer Productions & Publications
80. McClelland R (2013) Interview with Robert McClelland on the 50th Anniversary of the JFK Assassination - Part 1, Plast Reconstr Surg
81. Horne (2014) Altered History: Exposing Deceit and Deception in the JFK Assassination Medical Evidence Parts 1-5, The Future of Freedom Foundation, VA, USA
82. Junkkarinen B (1999) JFK Autopsy Photos Reviewed: What's Wrong With These Pictures? JFK Lancer Productions & Publications, 5 (4)
83. Custer JF (1997) Deposition of Jerrol Francis Custer, Assassination Records Review Board Deposition, October 28, Miller Reporting Company, Inc. Washington DC
84. Smith OC, Berryman HE, Lahren CH (1987) Cranial fracture patterns and estimate of direction from low velocity gunshot wounds. J Forensic Sci 32 (5). https://doi.org/10.1007/BF01355517
85. Assassination Records Review Board (1996) Testimony of Dr. James Joseph Humes
86. LSTC.H3_50TH_FAST Release (2012) Livermore Software Technology Corp. LSTC

87. Alvarez L (1976) A Physicist Examined the Kennedy Assassination Film, American Journal of Physics, 44 (9)
88. Nalli NR (2018) Gunshot-wound dynamics model for John F. Kennedy assassination, Heliyon 4 (4). https://doi.org/10.1016/j.heliyon.2018.e00831
89. Thompson J (1967) Six seconds in Dallas: A micro-study of the Kennedy assassination. New York: B. Geis Associates; distributed by Random House

Availability of data and material

All data and material for comparison associated with the current submission are available at
http://www.jfklancer.com/photos/autopsy_slideshow/
https://commons.wikimedia.org/wiki/File:Kennedy_autopsy_head.jpg
https://www.archives.gov/research/jfk/select-committee-report (exhibit F48 in HSCA Report)
http://www.history-matters.com/archive/contents/wc/contents_wh17.htm
https://hum3d.com/3d-models/lincoln-continental-x-100-1961/
https://www.lstc.com/products/models/dummies/H3_50th/ - LSTC.H3_50TH_FAST (2012)

Code availability

All code for simulation and analysis associated with the current submission is available at
https://www.lstc.com/products/ls-dyna/
https://www.altair.com/hyperworks/

Proof of permission

Available for images Figs.3a,b, Figs.9a,b and Figs.10a-c.